Electrocatalytic Oxygen Reduction by Cu Complexes of Tripeptide Derivatives of Glutathione

Profulla Mondol, Majid Hassani, Matthew J. Tucker,* and Christopher J. Barile*

Department of Chemistry, University of Nevada, Reno, Reno, NV 89557, USA

*E-mails: cbarile@unr.edu and matthewtucker@unr.edu

Abstract

The sluggishness of the oxygen reduction reaction (ORR) is the most significant challenge hindering fuel cell commercialization. Cu-based ORR catalysts are promising non-precious metal alternatives to Pt. In this manuscript, we synthesize four different Cu^{2+} complexes of tripeptides (Cu-GSHAmide, Cu-NCG, Cu-ECG and Cu-QCG) and develop relationships between their electrocatalytic activities and physicochemical properties. Rotating ring-disk electrode experiments indicate that the catalytic current densities and selectivities of the catalysts vary widely as a function of pH and peptide identity. Through FTIR spectroscopy, we describe the nature of the intermolecular forces between the peptides studied along with those of the corresponding Cu^{2+} complexes. This analysis allows us to quantify the degree of peptide aggregation in the ORR electrocatalysts. Combined with the Cu^{2+}-peptide binding constants, we develop models that accurately predict how peptide aggregation dictates catalyst current density and selectivity for the four-electron reduction of O_2 to water. These models indicate that Cu^{2+}-peptide ORR electrocatalysts with relatively strong binding constants and weak peptide aggregation exhibit increased selectivity and kinetics. This central finding highlights an important set of design rules for the development of future high-performance Cu ORR electrocatalysts.

Keywords: oxygen reduction, electrocatalysis, non-precious metal catalysts, copper catalysts, peptides, RRDE, FTIR

Introduction

The O_2 reduction reaction (ORR) is a central reaction in fuel cells, air batteries, and corrosion.[1–3] Although fuel cells have been used commercially since the 1960's, they have not been adopted on a large scale due to the slow kinetics and extensive overpotential of the ORR, which limits the energy efficiency and operating voltage of fuel cells. This large overpotential originates from the high strength of the O=O double bond (489 kJ/mol).[4]

A wide variety of different catalysts have been studied to decrease ORR overpotential. Pt-based ORR catalysts are the most successful with an overpotential of ~300 mV.[4–6] However, the high cost of Pt-based catalysts has prevented their widespread adoption. For this reason, a large amount of research has focused on the development of efficient non-precious metal ORR catalysts.[7–11] Biological systems indicate that it is possible to develop non-precious metal ORR catalysts that operate at low overpotentials. For example, laccase, a multicopper protein, exhibits diffusion-limited O_2 reduction with an overpotential of only ~70 mV.[12,13] Unfortunately, laccase is not stable over a wide pH range, and its large volume results in a low current density.[14–16]

The development of synthetic small-molecule Cu complexes is a promising strategy to produce inexpensive ORR catalysts with high current densities.[17–19] Anson and co-workers demonstrated that Cu complexes of 1,10-phenanthroline (phen) on graphite catalyze the four-electron reduction of O_2 to H_2O.[20–22] Chidsey and co-workers synthesized mononuclear Cu complexes with modified phen-based ligands and determined relationships between the electronic and steric properties of the ligands and the O_2 reduction performances.[23] Karlin and co-workers developed a mononuclear Cu(II) complex that efficiently catalyzes the four-electron reduction of O_2 to H_2O via a peroxodicopper(II) complex that is chemically reduced in the presence of decamethylferrocene.[24]

Our group recently investigated the ORR activities of Cu complexes of a simple tripeptide, glutathione (GSH).[25] In particular, we synthesized a ferrocene-modified glutathione that facilitates fast electron transfer to Cu, which results in higher selectivity for the four-electron reduction of O_2 to H_2O

than the unmodified Cu-GSH complex. These results imply that glutathione can serve as an appropriate scaffold for efficient Cu ORR catalysts if properly modified.

In this manuscript, to further pursue the strategy of using GSH as a research direction for creating active Cu ORR catalysts, we systematically study the relationship between tripeptide compositional relatives of GSH and the O_2 reduction activities of their Cu complexes. We rationalize the observed electrochemical trends by using physicochemical models that account for Cu^{2+}-peptide binding constants and molecular aggregation quantified using FTIR spectroscopy.

Methods

General Procedures

Peptide syntheses are described in the section below. All other chemicals were procured from commercial sources and used without purification. All electrochemical studies were performed using a VSP-300 Biologic potentiostat. A four-electrode cell was utilized in which modified glassy carbon served as the disc working electrode, Pt ring served as the ring electrode, a graphite rod functioned as the counter electrode, and a Ag/AgCl/3 M KCl (eDaq, Inc.) electrode was used as the counter electrode. Glassy carbon electrodes were polished using a suspension of 0.05 μm alumina followed by sonication for 8 min in water. The Pt ring electrodes (Pine Research Instrumentation, Inc.) were cleaned electrochemically in 15 mL of 0.1 M $HClO_4$ solution by cycling from -0.4 V to +1.7 V at 100 mV/s until the oxide stripping at ~0.35 mV remained constant.[19]

Peptide Synthesis

Glutathione Amide Synthesis: Glutathione amide (GSHAmide) was synthesized via a two-step process based on a slightly modified literature procedure.[26] Briefly, in the first step to form the monoethyl ester, 2 g of reduced glutathione (GSH) was dissolved in 25 mL of 1.8 M methanolic HCl. The mixture was continuously stirred for 3 hours at room temperature. The resulting solution was cooled at 0°C, and 180 mL of ice-cold diethyl ether was added. After letting the reaction mixture stand for 1.5 hours at 0°C, the ether was decanted. The precipitate was then washed two times with 60 mL of ice-cold water and dried

under reduced pressure. 1.8 g GSH-ester (90% yield) was produced in the first step. ^{1}H NMR (MeOD-d_4) δ 4.52 (t, 1H, CysCH), 4.02 (m, 3H, GlyCH_2, GluCH), 3.75 (s, 3H, -OCH_3), 2.91 (dd, 2H, CysCH_2), 2.57 (m, 2H, -$CH_2C\mathbf{H}_2CO$-), 2.20 (m, 2H, -$C\mathbf{H}_2CH_2CO$-). In the second step, which is an aminolysis reaction with ammonia, we followed the literature procedure to produce GSHAmide.

Syntheses of Other Peptides: Glutamic Acid-Cysteine-Glycine (ECG), Asparagine-Cysteine-Glycine (NCG), and Glutamine-Cysteine-Glycine (QCG): ECG, NCG, and QCG peptides were synthesized using standard Fmoc-protocols employing Knorr resin on a PS3 automated peptide synthesizer (Protein Technologies, Inc., Woburn, MA). The crude peptides were cleaved from the resin by addition of 92.5% trifluoroacetic acid (TFA), 2.5% distilled water, 2.5% triisopropylsilan, and 2.5% 1,2-ethanedithiol with stirring for 3 hours. Then, the peptides were purified by reverse-phase high-performance liquid chromatography (HPLC, Waters) using a Vydac C18 column and characterized by matrix-assisted laser desorption ionization (MALDI) mass spectroscopy (Bruker Microflex Daltonics, Inc., Billerica, MA). The residual TFA from the peptide cleavage and purification was then removed by subsequent reconstitutions with 0.1% HCl followed lyophilization. It should be noted that the total masses corresponding to QCG isotopes were also found at *m/z* 307.067, 308.045, 309.04, and *m/z* 310.037. A single peak corresponding to the total mass of NCG was observed at m/z 293.087. Note, the peaks corresponding to the isotopic distribution of the NCG peptide does not appear in the MALDI mass spectrum due to overlap with the matrix. The total mass and corresponding isotopic distribution of ECG was detected at *m/z* 308.028, 309.04, 310.037, and *m/z* 311.036 (Figure S1).

Binding Constant Determination

A Shimadzu UV-2550 spectrometer was used to measure the binding constants of Cu^{2+} to the various peptides. An aqueous peptide solution (0.4 mL of 2 mM except for GSHAmide, which was 10 mM) was used, and an aqueous $CuSO_4$ solution (0.5 M for ECG, 0.4 M for QCG and NCG, 0.1 M for GSHAmide) was added in intervals of 2.5 μL. UV-Vis absorbances were measured in the 200-500 nm range, and the absorbance peak at ~225 nm was plotted versus the number of equivalents of Cu^{2+} added.

To calculate the binding constants, fits to these plots were obtained using the single ligand binding saturation macro in SigmaPlot.

Electrochemical Experiments

Peptide (3.0 mg), $CuSO_4$ (3.0 mg), carbon (5.0 mg, Vulcan XC-72), and Nafion solution (30 μL, 5 wt %, D520, Fuel Cell Store, Inc.) were mixed and vortexed for 5 minutes. After vortexing, 5.0 mL MeOH was added, and the mixture was sonicated for 10 minutes to give a homogeneous suspension. About 80 μL of the suspension was drop cast on the glassy carbon electrode (5 mm in diameter) and dried using a custom-built upright rotator at a rotation speed of 8 rpm to ensure uniform film formation. This modified electrode was then used as the working electrode for rotating ring-disk electrode (RRDE) experiments using an electrode rotator (MSRX, Pine Research, Inc.). 1.2 M Britton-Robinson buffers (400 mM H_3BO_3, 400 mM H_3PO_4, 400 mM CH_3COOH) were used and adjusted to the desired pH using NaOH. Voltammetry was performed with 45 mL of buffer solution after it was sparged with O_2 for at least 10 minutes. Onset potentials were determined by calculating the voltage at which the current density for each voltammogram is equal to 10% of the current density at -1 V vs. Ag/AgCl. All reported error bars represent standard errors.

FTIR Experiments

Deuterium exchange of the amide residues was achieved by performing 2-3 reconstitutions in D_2O followed by lyophilization. Additional 1.2 M Britton-Robinson buffer solutions were prepared with $CuSO_4$ (6 mg of $CuSO_4$ in 10 mL buffer solution) and exchanged with D_2O. Following the final deuterium exchange, the samples were reconstituted in D_2O, sonicated for 15 minutes, and then filtered with a 0.2 μm syringe filter.

For the FTIR experiments, a stock solution for each peptide was prepared by dissolving ~20-30 mg of peptide in 10 mL of D_2O (~0.1 OD @ 1650 cm^{-1}). This stock solution was separated equally among twelve vials and lyophilized to maintain a similar amount of product in each container. Each

Cu^{2+} peptide complex and peptide alone was suspended in equal volumes of the prepared buffer solutions at different pHs and sonicated for 15 minutes.

FTIR spectra were obtained using a ThermoNicolet 6700 FTIR spectrometer equipped with a liquid nitrogen-cooled mercury cadmium telluride (MCT) detector. To collect higher sensitivity spectra and correct the baseline more accurately, the IR beam was routed into a home-built temperature-controlled setup.[27] A homemade CaF_2 sample holder was divided into two compartments with a 50 μm Teflon spacer for better background subtraction (i.e., buffer) under identical conditions. An automated translation stage moves the sample cell between the reference and the sample side collecting a single beam spectrum to account for drift and stability. All measurements were carried out in a nitrogen-purged chamber at ambient temperatures of 20°C. The sample and background spectra were averaged over 128 scans.

Modeling

FTIR data were utilized to quantify the total amount of peptide aggregation as a function of sequence as well as over a variety of pHs for each peptide alone and the Cu^{2+} peptide complexes. The vibrational spectra were decomposed into component peaks using a fitting method that included a sum of Gaussian functions, $y = A * e^{-4*\ln(2)*\frac{(x-x_c)^2}{w^2}}$, where x_c is the center frequency, A is the amplitude, and w is the full-width at half maximum (FWHM). Then, the total amount of aggregation was quantified by taking the product of the FWHM and the amplitude of the peaks at ~1620 cm^{-1} and ~1680 cm^{-1}, corresponding to anti-parallel beta sheets aggregates.[28–30] Linear combinations of the relative populations of each vibrational transition were screened during modeling, and a linear combination of 66% of the 1620 cm^{-1} and 34% of the 1680 cm^{-1} yielded the best-fit to the models.

Binding constants, which were obtained from UV-Vis spectra as described above, were measured at unadjusted pH. Binding constants could not be determined experimentally at different pH values due to the poor solubility of the Cu complexes in water. For this reason, the binding constants at different pH values were estimated by considering how the denticity of the peptide changes with pH.

The amine group (-NH_2) on the N-terminus of each peptide and the carboxylate group (COO^-) on peptides containing a glutamate residue, both of which readily bind to Cu^{2+}, were each considered to increase the denticity of the peptide by one vis-à-vis peptides that do not contain these groups or contain protonated forms of these groups (i.e. -NH_3^+ and –COOH). Binding constants at different pH values were then calculated assuming the binding constants increased by a factor of 100 per increase in denticity, which is a reasonable approximation for Cu^{2+} complexes of aminocarboxylate ligands.[31] The denticity values were adjusted at the various pH values according the relative populations of protonated and deprotonated forms according to the Henderson-Hasselbalch equation.

The aggregation and binding constant values were then normalized on a scale from 0 to 1. Similarly, the number of electrons transferred per mole of O_2 reduced as determined by RRDE and the logarithms of the maximum magnitude of the ORR currents measured during voltammetry per mole of catalyst were normalized on a scale from 0 to 1. The current per mole of catalyst was determined by first calculating the amount of catalyst loaded on each disc electrode. These values were determined by integrating the Cu(II)/Cu(I) redox couple measured during voltammetry under the assumption that each peptide binds to Cu in a 1:1 ratio, which has been demonstrated previously to be true for CuGSH and a related Cu tripeptide complex.[25] The maximum magnitude of ORR current was then divided by the calculated moles of Cu catalyst.

The models compared the normalized electrochemistry data to linear combinations of the normalized aggregation and binding constant values. Normalized values are referred to as “scores” from 0 to 1 throughout the manuscript. Each model consisted of a different linear combination with a weighting of $0 \leq x \leq 1$ for the aggregation values and a weighting of $0 \leq 1\text{-}x \leq 1$for the binding constant values. An increment of 1% was used for x to give 101 different sets of weighting values. For each of these 101 weighting values, positive and negative correlations were evaluated. In other words, four different sets of models were considered, those that compared the electrochemistry data to 1) increasing aggregation and increasing binding constant, 2) increasing aggregation and decreasing binding

constants, 3) decreasing aggregation and increasing binding constants, and 4) decreasing aggregation and decreasing binding constants. Therefore, in total, 404 (101 x 4) models were considered. For both the number of electron and current data, the selected best-fit models were the ones that possessed the lowest residues between the modeled values and experimental electrochemistry data.

Results and Discussion

Structure and Synthesis of Peptides

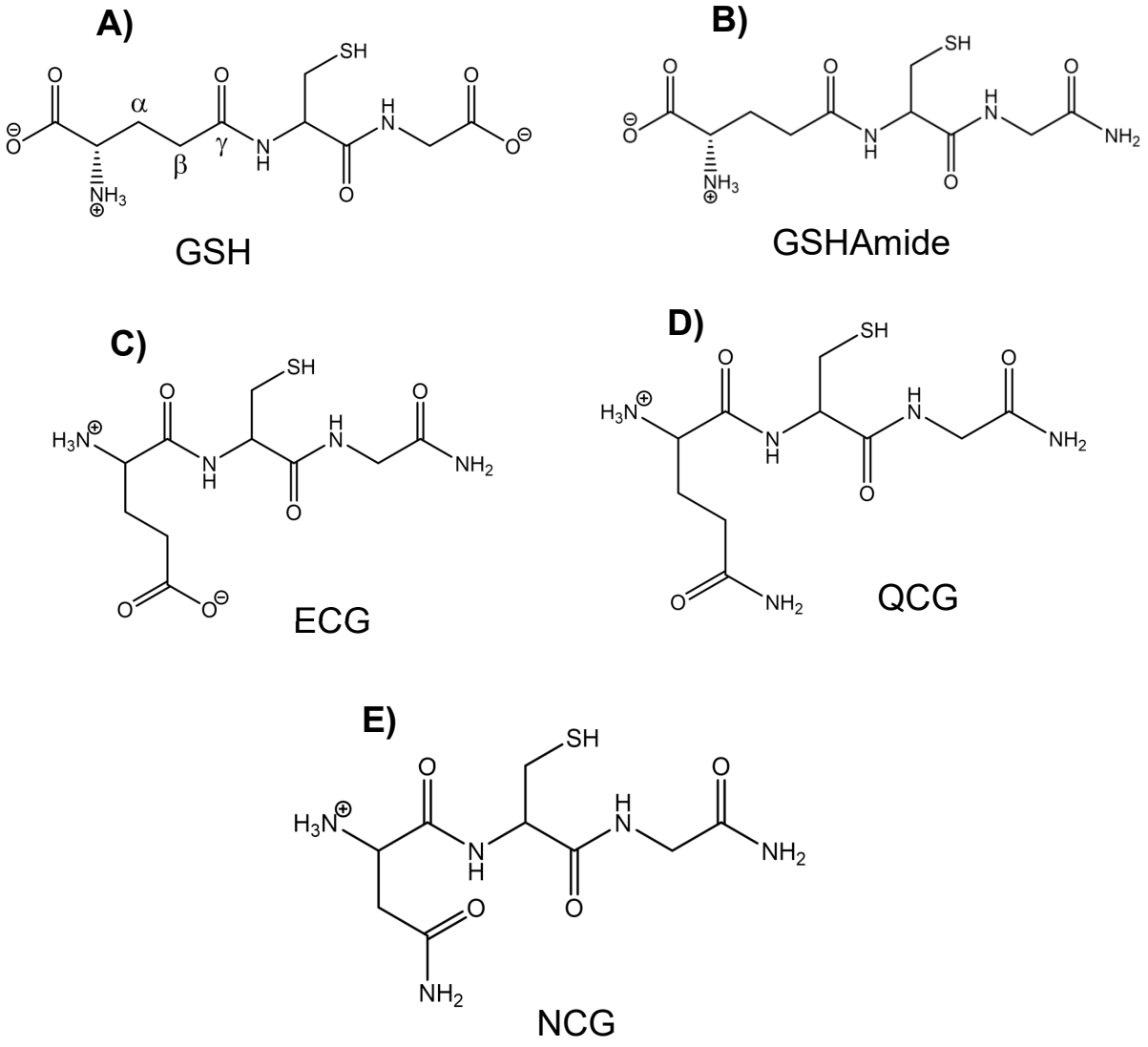

Figure 1: Predominant chemical structures of GSH (A), GSHAmide (B), ECG (C), QCG (D), and NCG (E) at neutral pH.

The Cu complexes of five different peptides were evaluated as ORR catalysts. The baseline catalyst is the previously studied Cu complex of glutathione (Cu-GSH). Glutathione is a tripeptide with a gamma linkage between the side chain of glutamate and the amine group of cysteine (Figure 1A). Three additional peptides in this work were synthesized using standard Fmoc-based solid-phase peptide synthesis with rink amide resin, which results in amidation of the C-terminal glycine residue (Figures 1C-1E). An additional peptide, GSH-carboyxamide (GSHAmide), was synthesized from the amidation

of the C-terminus of glutathione (Figure 1B). Together, the four amidated peptides allow for a fair set of comparison of catalytic activities for the Cu complexes. Previous studies demonstrate that the carboxylate on the glycine of glutathione does not bind to Cu^{2+}, and we therefore hypothesize that modification of the glycine with an amide would not significantly affect the Cu^{2+} binding constants of the peptides. Indeed, measurements discussed in detail later in the manuscript indicate that the binding constants of Cu-GSH and GSHAmide are similar. The Cu complex of ECG (Cu-ECG) was considered because ECG is a glutathione analog in which the glutamate residue is attached via a normal peptide linkage to cysteine instead of a gamma linkage (Figure 1C). We also evaluate Cu-QCG and Cu-NCG. QCG is a glutamine analog of ECG in which the carboxylate side chain is replaced by an amide (Figure 1D), and NCG (Figure 1E) contains one less methylene group on the sidechain than QCG. These peptides allow us to investigate the effects of carboxylate versus amide side chains of different lengths in the binding pocket of Cu^{2+} and the resulting effects on ORR catalysis.

Rotating Ring-Disc Electrochemistry

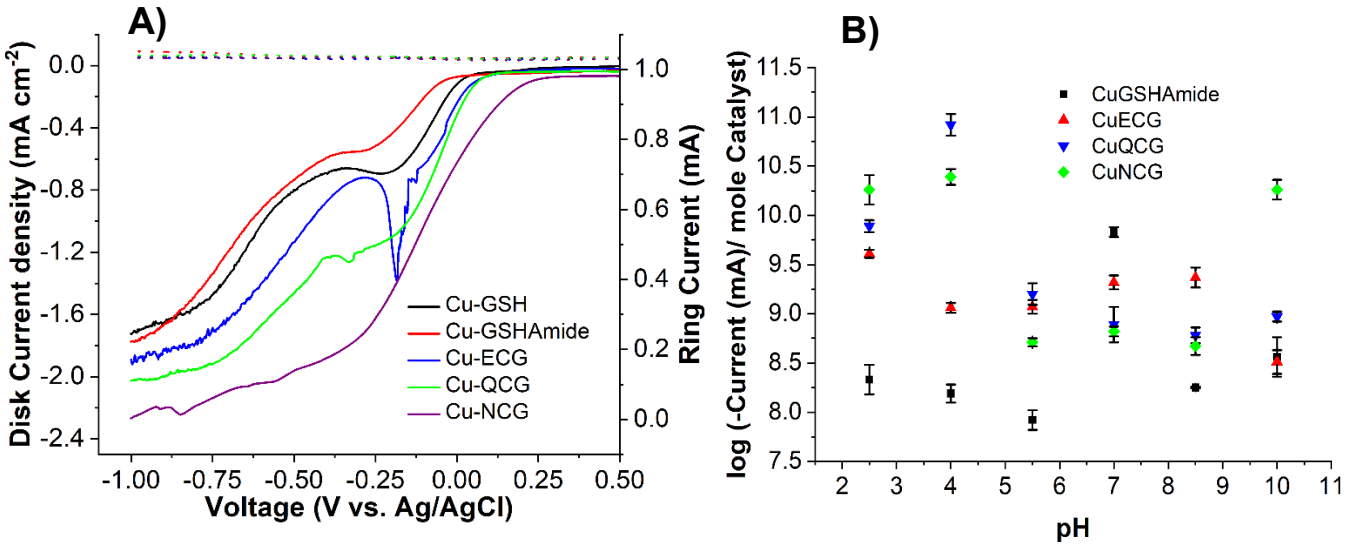

Figure 2: Electrocatalytic O_2 reduction by Cu-GSH (black line), Cu-GSHAmide (red line), Cu-ECG (blue line), Cu-QCG (green line) and Cu-NCG (purple line) in 1.2 M O_2-saturated Britton-Robinson Buffer at pH 5.5 using RRDE at 10 mV s^{-1} at 500 rpm. Solid line and dotted lines indicate the disk current density and ring current, respectively (A). Logarithms of maximum ORR cathodic current per mole of catalyst measured during RRDE for Cu-GSHAmide (black), Cu-ECG (red), Cu-QCG (blue), and Cu-NCG (green) at different pH values (B).

First, we investigated the ORR catalysis of different Cu^{2+}-peptide complexes by rotating ring-disc electrode (RRDE) experiments using O_2-saturated Britton-Robinson buffers at different pH values ranging from 2.5-10 (Figures S2-S9). For all catalysts studied and at all pH values, the ORR onset potentials for each Cu^{2+}-peptide complex were significantly more positive than those of the corresponding peptide without Cu (Table S1). These results indicate that Cu is needed to increase ORR activity. Representative RRDE plots for different Cu^{2+}-peptide complexes at pH 5.5 are displayed in Figure 2A. Among the five Cu^{2+}-peptide catalysts studied, there are significant differences in ORR activity. For example, the maximum cathodic ORR current density at -1.0 V vs. Ag/AgCl follows the order of Cu-NCG > Cu-QCG > Cu-ECG > Cu-GSHAmide ~ Cu-GSH. The observation that the disc voltammetry curves between Cu-GSHAmide and Cu-GSH are the most similar to one another is consistent with the interpretation that the active sites of the two catalysts are the same, and the modified glycine residue does not participate in Cu^{2+} binding. For this reason, we focus on relationships among the four catalysts with a C-terminal amide group (Cu-GSHAmide, CuECG, Cu-QCG, and Cu-NCG).

At this level of analysis, however, there is no obvious relationship between the structure of the five catalysts and their ORR current densities. In an attempt to determine the molecular origin of the differences in ORR current, we analyzed the measured currents on per mole of catalyst bases. The number of moles of catalyst in each case was calculated by integrating the Cu(II)/Cu(I) redox couple measured during voltammetry. We assumed that each peptide binds to Cu in a 1:1 ratio, which has been demonstrated previously to be true for CuGSH and a related Cu tripeptide complex.[25] At pH 5.5, the ORR currents per mole of catalyst follows the order of Cu-QCG > Cu-ECG > Cu-NCG > Cu-GSHAmide. Although this order is different than the raw current density data, there is still no obvious trend (e.g. carboxylate side chains vs. amide side chains) between peptide structure and current. The complete set of data at all pH values for each current per mole of catalyst is displayed in Figure 2B. Interestingly, the order of the currents across the five catalysts is different for each of the six pH values studied. These results suggest that there is a complicated relationship between catalyst activity, structure,

and pH. Later in this manuscript, we develop a model that takes into account Cu^{2+}-peptide binding strength and peptide aggregation to rationalize the observed trends in ORR current as a function of pH.

In addition to the changes in the RRDE disc currents across the five catalysts that are reflective of ORR activity, there are also significant differences in the RRDE ring currents, which are reflective of ORR selectivity.[32–34] In aqueous electrolytes, the ORR can occur via a four-electron reduction pathway to produce H_2O or a two-electron reduction pathway to produce H_2O_2. The one-electron reduction of O_2 to superoxide generally does not occur in aqueous systems.[35] In fuel cells, the four-electron pathway to H_2O is desired because it gives the highest voltage output, and the reactivity of H_2O_2 limits device durability. By comparing the ring and disc currents and accounting for the collection efficiency of the ring, the average number of electrons transferred per O_2 during ORR can be determined assuming only the two- and four-electron pathways are operative.

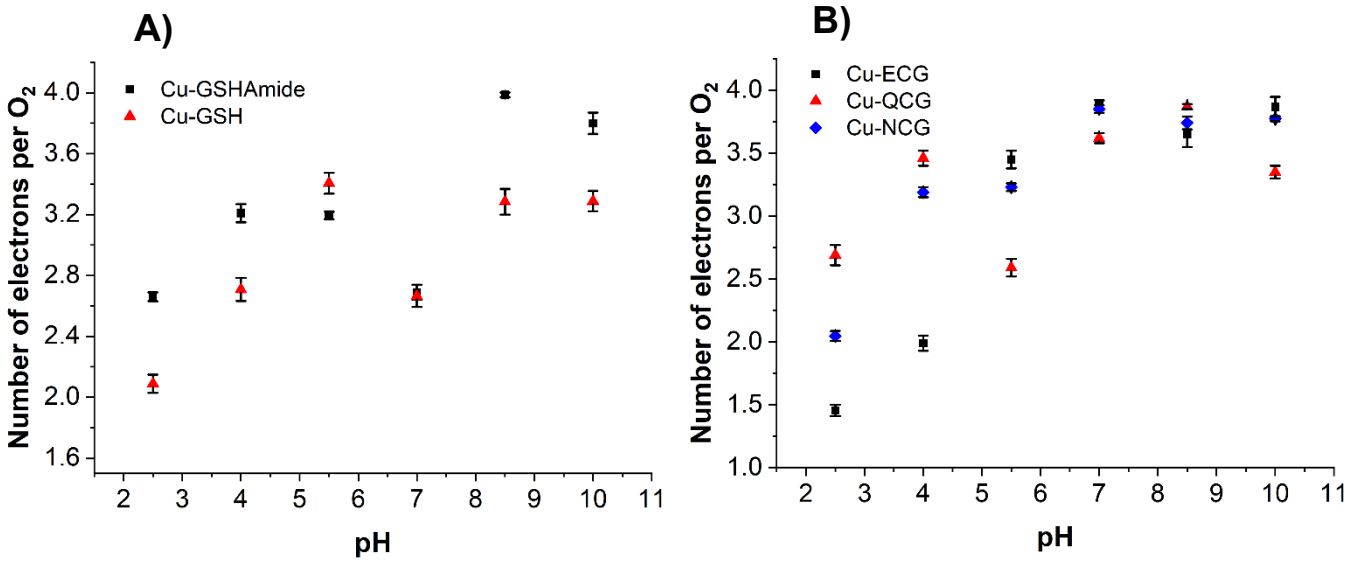

Figure 3: Number of electrons transferred per O_2 at -0.9 V vs. Ag/AgCl by Cu-GSHAmide (1A, black points), Cu-GSH (1A, red points), Cu-ECG (1B, black points), Cu-QCG (1B, red points), and Cu-NCG (1B, blue points) as calculated from RRDE experiments.

Figure 3 displays the average number of electrons transferred per O_2 as calculated from the RRDE experiments at -0.9 V vs. Ag/AgCl across all five Cu^{2+}-peptide catalysts and pH values. In general, the number of electrons transferred per O_2 increases with pH. This trend indicates that the selectivities of the Cu^{2+}-peptide catalysts for H_2O production increase in higher pH electrolytes.

Enhanced selectivity with increasing pH has been observed previously for other classes of molecular Cu and other ORR catalysts.[36-41] For both Cu-GSH and Cu-GSHAmide, the number of electrons transferred increases from pH 2.5 to pH 5.5, then slightly decreases at pH 7 before increasing at higher pH values (Figure 3A). The observation that the trends of Cu-GSH and Cu-GSHAmide for ORR selectivities are the same across pH further supports the notion that modification of the glycine residue outside the Cu^{2+}-binding pocket does not significantly affect ORR activity. The selectivities for the other three Cu^{2+} peptide catalysts also vary widely as a function of pH (Figure 3B). Notably, the number of electrons transferred for Cu-QCG at pH 4 is 3.46 ± 0.06, which is the highest value among the five catalysts at this pH. This result indicates that the Cu-QCG catalyst exhibits good selectivity for the four-electron reduction of O_2 to H_2O despite the low pH, which is uncommon for Cu-based ORR catalysts.[42,43]

Cu^{2+}-peptide Binding Measurements

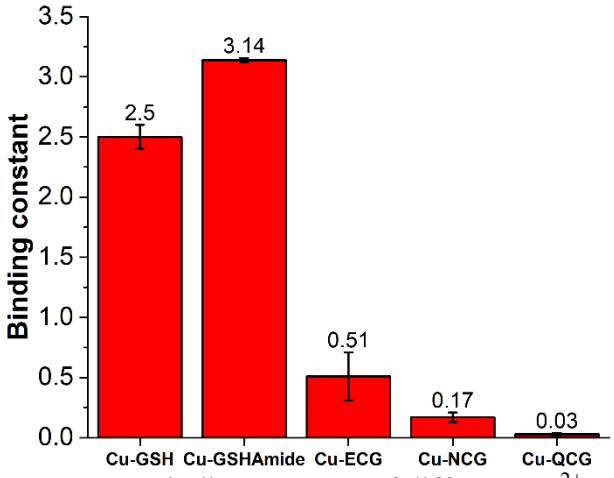

Figure 4: Binding constant of different Cu^{2+} peptide complexes.

In an attempt to understand the various relationships between pH, peptide structure, and catalyst performance, we first measured the Cu^{2+}-peptide binding constants using UV-Vis spectroscopy (Figures 4 and S10). Cu^{2+} binding to GSH is known to occur in a pocket that involves the thiol group of cysteine and the carboxylate and amine of glutamate. We find that the Cu^{2+}-binding constants to GSH and GSHAmide are similar, which is expected given that the two peptides only differ in whether or not the glycine residue, which is not directly involved in binding, contains an amide cap. In contrast, the Cu^{2+}-binding constant to ECG is significantly smaller than that of GSHAmide. Although the structures of

these two peptides are similar, ECG contains a normal glutamate linkage, while GSHAmide contains a gamma glutamate linkage. This difference causes the amine group of the glutamate residue, which is protonated at neutral pH, to be closer to the thiol on the cysteine in ECG. Because protonated amines do not bind to Cu^{2+} due to electrostatic repulsion, this effect results in a decreased binding constant for Cu-ECG as compared to Cu-GSHAmide. Furthermore, the Cu^{2+}-binding constants for QCG and NCG are the lowest among all five Cu complexes. The weaker binding constants for these two peptides arise from the lack of carboxylate on the side chain of the N-terminal residue. In the other three Cu complexes, the carboxylate binds to Cu^{2+}, leading to increased binding constants. Lastly, the Cu^{2+}-binding constant to QCG is significantly lower than to NCG due to differences in the distance of the amide side chain to the Cu^{2+}-binding site. The amide is further away from the Cu^{2+}-binding site in QCG, which decreases the overall binding constant.

Infrared Spectroscopy and Peptide Aggregation

In addition to evaluating Cu^{2+}-peptide binding constants, we utilized infrared spectroscopy to quantify the total peptide aggregation as the main peptide structural component. Since the amide I absorption band is primarily derived from backbone carbonyl stretching vibrations with some NH bending, it has been extensively used to characterize the amount of native structure present in protein and peptide systems including aggregation.[42-44] This sensitivity to peptide structure results from the excitonic coupling of the carbonyl modes along the backbone,[45,46] hydrogen bonding,[47] and degrees of hydration.[48,49] Upon aggregation, it is therefore expected that the peptide stacking, increased hydrogen bonding, and the degree of exposure to water of the amide group of the peptide will have a profound effect on, not only the vibrational frequency of the amide I, but also the FWHM of the observed peaks.

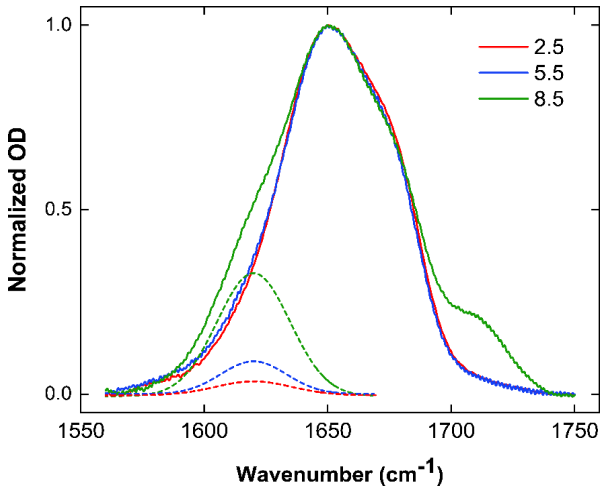

Figure 5: Representation of typical normalized infrared spectrum of peptide complexes, Cu^{2+}-NCG. The dotted lines demonstrate the increase of the aggregation peak, 1629 cm^{-1}, at the indicated pH values.

Two of the main absorption bands, observed at ~1620 cm^{-1} and ~1680 cm^{-1} in the infrared spectrum, correspond to the formation of in-phase and out-of-phase anti-parallel β-sheets, respectively. The vibrational frequency and amplitude of the transition at ~1680 cm^{-1} are not sensitive to the size of the sheets. However, the opposite is true of the ~1620 cm^{-1} band, which is sensitive to the dimensions of the sheets.[29,50,51] This effect is largely due to the in-phase oscillation of the residues in-register between strands having a transition dipole perpendicular to the β-strands.[51] To quantify the amount of aggregation present, the parameters associated with these two absorption bands are determined by Gaussian peak fitting of the infrared spectrum. Although both absorption bands are often present in the infrared spectrum of aggregates, it appears that out-of-phase anti-parallel β-sheets were more pronounced in the spectra of the peptide alone, while the infrared spectra of the peptide bound to the Cu^{2+} in the complex showed more in-phase anti-parallel β-sheets.

In Figure 5, the fitting of the lower frequency aggregation band as a function of pH is shown for the Cu-NCG complex in D_2O exchanged Britton-Robinson buffer solution. The total peak fitting (see supporting information) reveals three distinct absorption bands: the two aggregation bands at ~1620 cm^{-1} and ~1680 cm^{-1} with another absorption band at ~1650 cm^{-1} due to the presence of random coil.[43,52] Additionally, two smaller absorption bands are observed at ~1710 cm^{-1} and <1600 cm^{-1} originating from the carboxylic group protonation and deprotonation states, respectively. The infrared

spectra of the GSHAmide, ECG, and QCG peptides exhibited similar number of peaks at the same frequencies, but different amplitudes and FWHM for the varying levels of aggregation. The fittings for the peptides alone and the Cu^{2+}-peptide complexes at different pHs are shown in Figures S11-S22.

According to aggregation analysis of QCG, NCG, ECG, and GSHAmide peptides alone (without Cu^{2+} present), the absorption bands, observed at ~1680 cm^{-1} and ~1620 cm^{-1}, clearly show a dependence on pH. At an initial pH, the infrared spectrum of each peptide was divided into Gaussian components via least squares fitting. Then, the peptide aggregation level was quantified by fixing the vibrational frequencies of the peaks for all amide I transitions and varying the amplitude and FWHM of each peak for a given pH (Figures S23-S24). When the pH was decreased from 10 to 2.5 for the NCG, QCG, and ECG peptides, an increase in intensity of the out-of-phase antiparallel β-sheet transition, 1680 cm^{-1}, was observed (Figure S25B). However, the 1620 cm^{-1} transition remained mostly invariant, likely due to the peptides in solution forming small sized less ordered aggregates (Figure S25A).[51] NCG demonstrates the most sensitivity to pH changes followed by ECG, while QCG had the least variation as well as the least total aggregation population. These results indicate that the aggregate formation is likely aided by the neutralization of the charges on the sidechains at lower pHs for easier β-strand stacking despite steric effects of the longer sidechains. On the other hand, the shorter asparagine (N) sidechain of NCG acts as another possible hydrogen bond to stabilize the β-sheet stacking.

In contrast to NCG, QCG, and ECG peptides, the infrared spectra of the GSHAmide peptide displays in-phase aggregation at ~1620 cm^{-1} without the presence of the 1680 cm^{-1} absorption band. This result suggests that the gamma linkage may allow for better stacking of the β sheets in solution and provides better ordering of hydrogen bonding. As further evidence of this phenomenon, the GSHAmide peptide aggregation showed reverse dependence on change of pH, increasing significantly with higher pH. As in the NCG above, the higher pH would afford more in-register hydrogen bonding across the gamma linkage providing better β-strand stacking. In general, Figure S26 illustrates the highest total

aggregation population of each peptide in solution varies in the following way: GSHAmide > NCG > ECG > QCG. This overall trend coincides with the physical interpretations discussed above.

In the presence of Cu^{2+}, the peptides undergo significant changes in the types of aggregates formed, indicated by the increase in the absorption band at ~1620 cm^{-1}. As mentioned above, the amplitudes of the 1620 cm^{-1} transitions signify the presence of a much larger size and ordered β-strand stack.[51] The ability of the metals to trigger aggregation formation is not uncommon, especially for Cu^{2+} ions.[53-56] Using a similar aggregation analysis as above, the Cu^{2+}-peptide complexes were assessed for the total population aggregation. In QCG, ECG, and NCG Cu^{2+}-peptide complexes, the in-phase beta-sheet (frequency distributions at ~1620 cm^{-1}) increases as the pH increases with the exception of ECG. Cu-ECG, due to the repulsive effect of the carboxylate sidechain at high pH, demonstrates the most aggregation at lower pH. The 1680 cm^{-1} aggregation band remains relatively independent of the protonation states of surrounding solvent molecules. Cu-ECG demonstrates the most sensitivity to pH as observed in this high frequency aggregation band due to the removal of the charge of the carboxylate sidechain leading to the highest total aggregation population at low pH (Figure S23C).

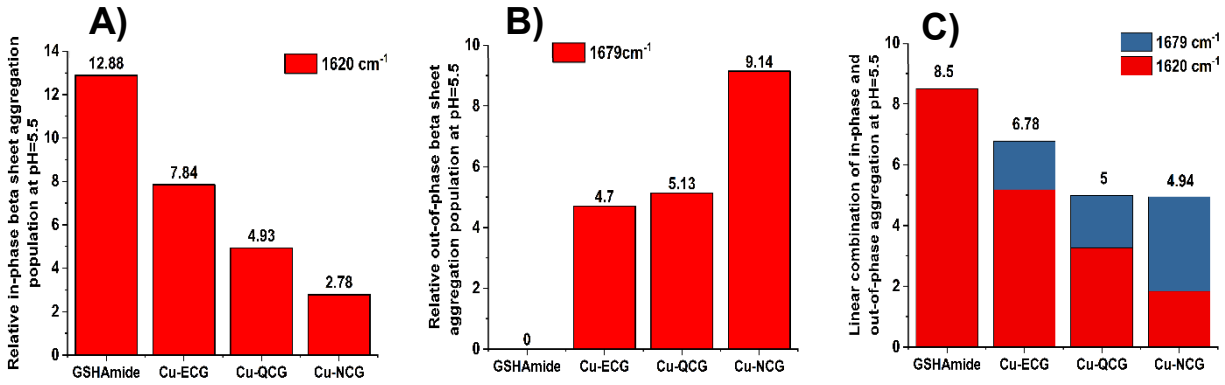

Figure 6: Relative aggregation analysis for Cu^{2+}-peptide complexes at pH=5.5

To compare the total aggregation population in the all Cu^{2+}-peptide complexes, the percentages (i.e. coefficients) of each contributing aggregation band were obtained from the model of the catalytic behavior. A resultant linear combination of 66% and 34% of the two aggregation bands were used to assess the overall trends in total aggregation population at pH = 5.5 (Figure 6C) (other pHs are shown in

Figures S23C and S24C). This analysis at pH = 5.5 indicates the following ordering of total aggregation population: Cu-GSHAmide > Cu-ECG > Cu-QCG > Cu-NCG (Figure 6C). However, the Cu^{2+}-NCG peptide displayed the highest aggregation potential overall at high pH (Figure S24C), while the Cu^{2+}-GSHAmide was equally large independent of the pH (Figure S23C and S24C). This trend is similar to the peptides alone, and overall expected because the gamma linkage and the shorter sidechain would likely enhance the in-register hydrogen bonding during stacking. The Cu^{2+}-ECG has the next largest aggregation population at the lowest pH, which becomes inhibited at higher pHs due to repulsion of the carboxylate. Lastly, the Cu-QCG tends to be the least prone to aggregation.

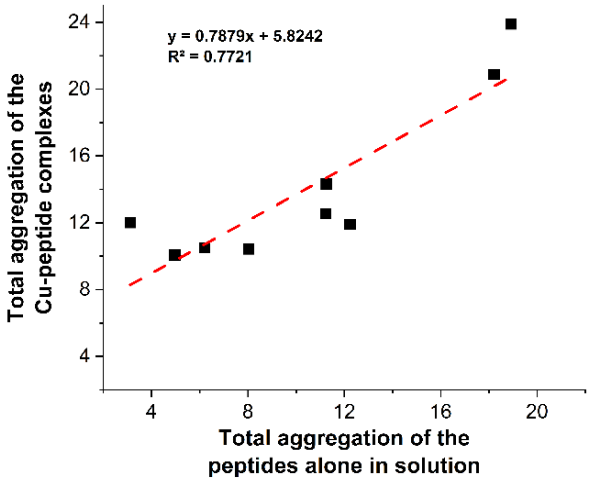

Figure 7: Total aggregation population of the Cu^{2+}-peptide complexes vs total aggregation population of the peptide alone

Finally, after understanding the above trends of the peptides with sequence and pH, we wanted to determine if the aggregation of the peptides in solution correlated to the total aggregation population of the Cu^{2+}-peptide complexes. As seen in Figure 7, a clear trend was observed between the smaller unordered solution phase aggregates and the larger ordered aggregates found in the Cu^{2+}-peptide complexes. Figure 7 was produced by applying point for point analysis of each peptide starting at the highest aggregation population found in solution versus the highest total aggregation population found in the complex. Then, the next highest aggregation points were added to the plot and so on. This linear correlation plot indicates that the short peptides can first be assessed for their likelihood to aggregate in

solution alone to screen the one most advantageous ones for catalytic behavior. For example, later in this manuscript, we demonstrate how a model accounting for catalyst aggregation is a good predictor of catalytic current. Ultimately, these relationships between peptide aggregation, Cu^{2+}-peptide complex aggregation, and catalyst activity could allow for a reduction in the number of systems needed for screening to discover new active catalysts.

Modeling Catalyst Performance

Considering both the Cu^{2+}-binding constants and aggregation of the Cu^{2+}-peptide complexes, we now seek to understand the physicochemical origins of the various electrocatalytic activities of the Cu^{2+}-peptide catalysts in different pH buffers. To more readily identify possible trends between catalytic activity, binding constants, and the degrees of complex aggregation, we quantified all of these attributes on a normalized scale from 0 to 1 across the four Cu complexes with C-terminal amide-capped peptides and across varying pH. For Cu^{2+}-binding constants and complex aggregation metrics, a value of 0 represents the weakest binding constant and smallest amount of aggregation, while a value of 1 represents the strongest binding constant and largest quantity of aggregation. Similarly, electrocatalytic ORR metrics were also normalized. A value of 0 represents the lowest selectivity for H_2O production and the lowest current on a per catalyst basis, while a value of 1 represents the highest selectivity for H_2O production and the highest current on a per catalyst basis. We call these sets of normalized values "scores."

When considered individually, there is no evident correlation between catalyst selectivity scores or catalyst current scores and binding constant scores or aggregation scores. For this reason, we considered linear combinations of binding constant and aggregation scores to model the electrochemical data. Specifically, we considered all possible linear combinations of binding constant and aggregation scores with weighting values in increments of 1% for both catalyst selectivity and catalyst current (see the "Modeling" portion of the "Experimental" section for more details).

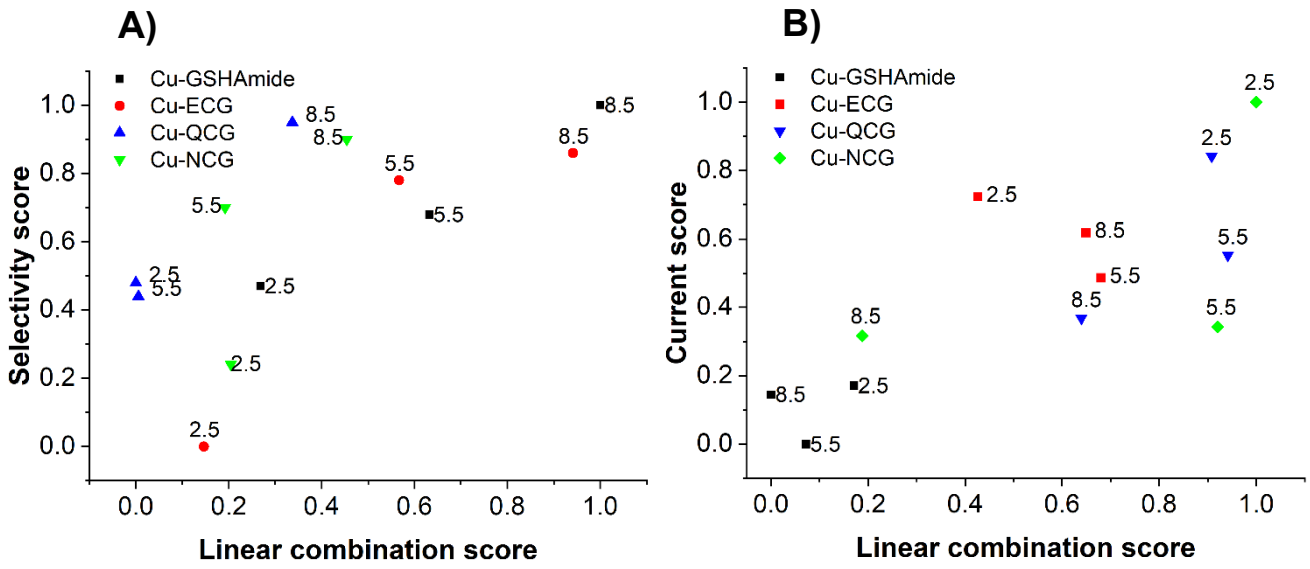

Figure 8: Comparison of catalyst ORR selectivity scores (A) and ORR current scores (B) of the four Cu complexes with C-terminal amide-capped peptides at various pH values and scores calculated from best-fit models that account for the strength of Cu^{2+} binding and peptide aggregation.

For catalyst selectivity, the best-fit model is a linear combination consisting of a 89% weighting for the binding constant scores and a 11% weighting for the aggregation scores. In this model, the binding constants increase as the selectivities increase, and the degrees of aggregation decrease as the selectivities increase. For catalyst current, the best-fit model is a linear combination consisting of a 16% weighting for the binding constant scores and a 84% weighting for the aggregation scores. In this model, both the binding constants and the degrees of aggregation decrease as the currents increase. These two models based on binding constant and aggregation fairly accurately predict catalyst selectivity and catalyst current (Figure 8).

Aside from being predictive of electrocatalytic activity, the results of these two models can be rationalized from a physical chemistry perspective. First, the selectivity model suggests that well-defined Cu complexes with stronger Cu^{2+}-binding constants that are relatively non-aggregated possess a narrower range of reactivity, which results in more selective ORR catalysis (Figure 8A). Second, the current model suggests that loose binding and less aggregation allows for fast electron transfer, which enhances catalytic current (Figure 8B). In other words, tightly bound Cu adducts have a lower

propensity to bind to O_2, which decreases current. Similarly, more aggregated active sites could both decrease O_2 mass transfer and decrease electron transfer, also decreasing current.

Design Rules for Cu^{2+}-peptide ORR Catalysts

These models give rise to important and clear design rules for promising ORR fuel cell catalysts based on Cu^{2+}-peptide complexes that are both highly selective for the four-electron reduction of O_2 to water and that can operate at high rates. To design selective catalysts, complexes with relatively strong Cu^{2+} binding constants and weak peptide aggregation should be targeted. This set of design rules should also lead to catalysts that display relatively fast ORR kinetics. Even though strong Cu^{2+} binding constants are predicted to decrease catalytic current density, the weighting factor of the current density model as it relates to binding is small (16%), and so the advantageous effect of weak peptide aggregation in promoting catalytic current should outweigh the detrimental effect of tighter binding. In other words, our results imply that researchers should target Cu^{2+}-peptide complexes with strong binding constants and weak peptide aggregation to further develop a promising class of non-precious metal ORR catalysts that simultaneously exhibit high selectivity and fast kinetics.

Conclusions

A series of novel Cu^{2+} complexes of tripeptides, inspired by glutathione, were investigated as electrocatalytic ORR catalysts using rotating ring-disk electrochemistry. Using binding constant measurements and quantitative peptide aggregation measurements obtained from infrared spectroscopy, we explain trends in both the selectivities and current densities of the Cu^{2+}-peptide electrocatalysts. In particular, our modeling indicates that Cu^{2+}-peptide complexes with relatively strong binding constants and weak peptide aggregation facilitates fast and selective catalyst formation for the four-electron reduction of O_2 to water. We anticipate that this fundamental insight into catalyst design should aid in the development of future highly-active non-precious metal ORR electrocatalysts based on molecular Cu complexes.

Supporting Information

MALDI data, Rotating ring disk electrochemistry data, UV-visible spectroscopy data, and FTIR data.

Author Information

Corresponding Author

*Email: cbarile@unr.edu and matthewtucker@unr.edu

ORCID

Christopher J. Barile: 0000-0002-4893-9506

Mathew J. Tucker: 0000-0001-9724-4455

Notes

The authors declare no competing interests.

Acknowledgments

C.J.B. and P.M. acknowledge that this material is based upon work supported by the National Science Foundation (NSF) CAREER Award under Grant No. CHE2046105. M.J.T. and M.H. acknowledges the NSF for the financial support of this work through CHE-2102275. The authors acknowledge the Shared Instrumentation Laboratory in the Department of Chemistry at UNR.

References

(1) Ghobadi, S.; Işıkel Şanlı, L.; Bakhtiari, R.; Alkan Gürsel, S. Green Composite Papers via Use of Natural Binders and Graphene for PEM Fuel Cell Electrodes. *ACS Sustain. Chem. Eng.* **2017**, *5*, 8407–8415.

(2) Carrette, L.; Friedrich, K. A.; Stimming, U. Fuel Cells: Principles, Types, Fuels, and Applications. *ChemPhysChem* **2000**, *1*, 162–193.

(3) Prater, K. B. Polymer Electrolyte Fuel Cells: A Review of Recent Developments. *J. Power Sources* **1994**, *51*, 129–144.

(4) Gewirth, A. A.; Thorum, M. S. Electroreduction of Dioxygen for Fuel-Cell Applications: Materials and Challenges. *Inorg. Chem.* **2010**, *49*, 3557–3566.

(5) Gasteiger, H. A.; Panels, J. E.; Yan, S. G. Dependence of PEM Fuel Cell Performance on Catalyst Loading. *J. Power Sources* **2004**, *127*, 162–171.

(6) Gasteiger, H. A.; Kocha, S. S.; Sompalli, B.; Wagner, F. T. Activity Benchmarks and Requirements for Pt, Pt-Alloy, and Non-Pt Oxygen Reduction Catalysts for PEMFCs. *Appl. Catal. B Environ.* **2005**, *56*, 9–35.

(7) Bashyam, R.; Zelenay, P. A Class of Non-Precious Metal Composite Catalysts for Fuel Cells. *Nature* **2006**, *443*, 63–66.

(8) Jaouen, F.; Lefèvre, M.; Dodelet, J.-P.; Cai, M. Heat-Treated Fe/N/C Catalysts for O_2 Electroreduction: Are Active Sites Hosted in Micropores? *J. Phys. Chem. B* **2006**, *110*, 5553–5558.

(9) Wang, B.; Feng, J.; Gao, C. Surface Wettability of Compressed Polyelectrolyte Multilayers. *Colloids Surf. Physicochem. Eng. Asp.* **2005**, *259*, 1–5.

(10) Jaouen, F.; Dodelet, J.-P. O_2 Reduction Mechanism on Non-Noble Metal Catalysts for PEM Fuel Cells. Part I: Experimental Rates of O_2 Electroreduction, H_2O_2 Electroreduction, and H_2O_2 Disproportionation. *J. Phys. Chem. C* **2009**, *113*, 15422–15432.

(11) Matter, P. H.; Ozkan, U. S. Non-Metal Catalysts for Dioxygen Reduction in an Acidic Electrolyte. *Catal. Lett.* **2006**, *109*, 115–123.

(12) Schweiger, H.; Vayner, E.; Anderson, A. B. Why Is There Such a Small Overpotential for O_2 Electroreduction by Copper Laccase? *Electrochem. Solid-State Lett.* **2005**, *8*, A585.

(13) Mano, N.; Soukharev, V.; Heller, A. A Laccase-Wiring Redox Hydrogel for Efficient Catalysis of O2 Electroreduction. *J. Phys. Chem. B* **2006**, *110*, 11180–11187.

(14) Shleev, S.; Tkac, J.; Christenson, A.; Ruzgas, T.; Yaropolov, A. I.; Whittaker, J. W.; Gorton, L. Direct Electron Transfer between Copper-Containing Proteins and Electrodes. *Biosens. Bioelectron.* **2005**, *20*, 2517–2554.

(15) Hussein, L.; Rubenwolf, S.; Stetten, F. von; Urban, G.; Zengerle, R.; Krueger, M.; Kerzenmacher, S. A Highly Efficient Buckypaper-Based Electrode Material for Mediatorless Laccase-Catalyzed Dioxygen Reduction. *Biosens. Bioelectron.* **2011**, *26*, 4133–4138.

(16) Zloczewska, A.; Jönsson-Niedziolka, M.; Rogalski, J.; Opallo, M. Vertically Aligned Carbon Nanotube Film Electrodes for Bioelectrocatalytic Dioxygen Reduction. *Electrochimica Acta* **2011**, *56*, 3947–3953.

(17) Gautam, R. P.; Lee, Y. T.; Herman, G. L.; Moreno, C. M.; Tse, E. C. M.; Barile, C. J. Controlling Proton and Electron Transfer Rates to Enhance the Activity of an Oxygen Reduction Electrocatalyst. *Angew. Chem. Int. Ed.* **2018**, *57*, 13480–13483.

(18) Tse, E. C. M.; Barile, C. J.; Kirchschlager, N. A.; Li, Y.; Gewargis, J. P.; Zimmerman, S. C.; Hosseini, A.; Gewirth, A. A. Proton Transfer Dynamics Control the Mechanism of O_2 Reduction by a Non-Precious Metal Electrocatalyst. *Nat. Mater.* **2016**, *15*, 754–759.

(19) Barile, C. J.; Tse, E. C. M.; Li, Y.; Sobyra, T. B.; Zimmerman, S. C.; Hosseini, A.; Gewirth, A. A. Proton Switch for Modulating Oxygen Reduction by a Copper Electrocatalyst Embedded in a Hybrid Bilayer Membrane. *Nat. Mater.* **2014**, *13*, 619–623.

(20) Lei, Y.; Anson, F. C. Dynamics of the Coordination Equilibria in Solutions Containing Copper(II), Copper(I), and 2,9-Dimethyl-1,10-Phenanthroline and Their Effect on the Reduction of O_2 by Cu(I). *Inorg. Chem.* **1995**, *34*, 1083–1089.

(21) Lei, Y.; Anson, F. C. Mechanistic Aspects of the Electroreduction of Dioxygen as Catalyzed by Copper-Phenanthroline Complexes Adsorbed on Graphite Electrodes. *Inorg. Chem.* **1994**, *33*, 5003–5009.

(22) McCrory, C. C.; Devadoss, A.; Ottenwaelder, X.; Lowe, R. D.; Stack, T. D. P.; Chidsey, C. E. Electrocatalytic O_2 Reduction by Covalently Immobilized Mononuclear Copper (I) Complexes: Evidence for a Binuclear Cu_2O_2 Intermediate. *J. Am. Chem. Soc.* **2011**, *133*, 3696–3699.

(23) McCrory, C. C. L.; Ottenwaelder, X.; Stack, T. D. P.; Chidsey, C. E. D. Kinetic and Mechanistic Studies of the Electrocatalytic Reduction of O_2 to H_2O with Mononuclear Cu Complexes of Substituted 1,10-Phenanthrolines. *J. Phys. Chem. A* **2007**, *111*, 12641–12650.

(24) Fukuzumi, S.; Kotani, H.; Lucas, H. R.; Doi, K.; Suenobu, T.; Peterson, R. L.; Karlin, K. D. Mononuclear Copper Complex-Catalyzed Four-Electron Reduction of Oxygen. *J. Am. Chem. Soc.* **2010**, *132*, 6874–6875.

(25) Mondol, P.; Barile, C. J. Four-Electron Electrocatalytic O_2 Reduction by a Ferrocene-Modified Glutathione Complex of Cu. *ACS Appl. Energy Mater.* **2021**, *4*, 9611–9617.

(26) Anderson, M. E.; Powrie, F.; Puri, R. N.; Meister, A. Glutathione Monoethyl Ester: Preparation, Uptake by Tissues, and Conversion to Glutathione. *Arch. Biochem. Biophys.* **1985**, *239*, 538–548.

(27) Chalyavi, F.; Hogle, D. G.; Tucker, M. J. Tyrosine as a Non-Perturbing Site-Specific Vibrational Reporter for Protein Dynamics. *J. Phys. Chem. B* **2017**, *121*, 6380–6389.

(28) Cheatum, C. M.; Tokmakoff, A.; Knoester, J. Signatures of β-Sheet Secondary Structures in Linear and Two-Dimensional Infrared Spectroscopy. *J. Chem. Phys.* **2004**, *120*, 8201–8215.

(29) Demirdöven, N.; Cheatum, C. M.; Chung, H. S.; Khalil, M.; Knoester, J.; Tokmakoff, A. Two-Dimensional Infrared Spectroscopy of Antiparallel β-Sheet Secondary Structure. *J. Am. Chem. Soc.* **2004**, *126*, 7981–7990.

(30) Ganim, Z.; Chung, H. S.; Smith, A. W.; DeFlores, L. P.; Jones, K. C.; Tokmakoff, A. Amide I Two-Dimensional Infrared Spectroscopy of Proteins. *Acc. Chem. Res.* **2008**, *41*, 432–441.

(31) Martell, A. E. Chelating Agents for Metal Buffering and Analysis in Solution. **1978**, *50*, 813–829.

(32) Sunarso, J.; Torriero, A. A. J.; Zhou, W.; Howlett, P. C.; Forsyth, M. Oxygen Reduction Reaction Activity of La-Based Perovskite Oxides in Alkaline Medium: A Thin-Film Rotating Ring-Disk Electrode Study. *J. Phys. Chem. C* **2012**, *116*, 5827–5834.

(33) Jung, E.; Shin, H.; Lee, B.-H.; Efremov, V.; Lee, S.; Lee, H. S.; Kim, J.; Hooch Antink, W.; Park, S.; Lee, K.-S. Atomic-Level Tuning of Co–N–C Catalyst for High-Performance Electrochemical H2O2 Production. *Nat. Mater.* **2020**, *19*, 436–442.

(34) Lu, Z.; Chen, G.; Siahrostami, S.; Chen, Z.; Liu, K.; Xie, J.; Liao, L.; Wu, T.; Lin, D.; Liu, Y. High-Efficiency Oxygen Reduction to Hydrogen Peroxide Catalysed by Oxidized Carbon Materials. *Nat. Catal.* **2018**, *1*, 156–162.

(35) Song, C.; Zhang, J. Electrocatalytic Oxygen Reduction Reaction. In *PEM Fuel Cell Electrocatalysts and Catalyst Layers: Fundamentals and Applications*; Zhang, J., Ed.; Springer London: London, **2008**, 89–134.

(36) Noffke, B. W.; Li, Q.; Raghavachari K.; Li, L. A Model for the pH-Dependent Selectivity of the Oxygen Reduction Reaction Electrocatalyzed by N-Doped Graphitic Carbon. *J. Am. Chem. Soc.* **2016**, *138*, 13923–13929.

(37) Bai, J.; Zhu, Q.; Lv, Z.; Dong, H.; Yu, J.; Dong, L. Nitrogen-doped graphene as catalysts and catalyst supports for oxygen reduction in both acidic and alkaline solutions *Int. J. Hydrog. Energy* **2013**, *38*, 1413–1418.

(38) Iwazaki, T.; Oninata, R.; Sugimoto, W.; Takasu, Y. High oxygen-reduction activity of silk-derived activated carbon. *Electrochem. Commun.* **2009**, *11*, 376–378.

(39) Park, J.; Nabae, Y.; Hayakawa, T. Kakimoto, M. Highly selective twoelectron oxygen reduction catalyzed by mesoporous nitrogen-doped carbon. *ACS Catal.* **2014**, *4*, 3749–3754.

(40) Thorseth, M. A.; Letko, C. S.; Tse, E. C. M.; Rauchfuss, T. B.; Gewirth, A. A. Ligand effects on the overpotential for dioxygen reduction by tris (2-pyridylmethyl) amine derivatives. *Inorg. Chem.* **2013**, *52*, 628-634.

(41) Thorseth, M. A.; Tornow, C. E.; Tse, E. C. M.; Gewirth, A. A. Cu complexes that catalyze the oxygen reduction reaction *Coord. Chem. Rev.* **2013**, *257*, 130-139.

(42) Ghosh, A.; Tucker, M. J. Gai, F. 2D IR Spectroscopy of Histidine: Probing Side-Chain Structure and Dynamics via Backbone Amide Vibrations. *J. Phys. Chem. B* **2014**, *118*, 7799–7805.

(43) DeFlores, L. P.; Ganim, Z. Nicodemus, R. A.; Tokmakoff, A. Amide I′−II′ 2D IR Spectroscopy Provides Enhanced Protein Secondary Structural Sensitivity. *J. Am. Chem. Soc.* **2009**, *131*, 3385–3391.

(44) Barth, A.; Zscherp, C. What vibrations tell about proteins *Q. Rev. Biophys.* **2002**, *35*, 369–430.

(45) Buchanan, L. E.; Carr, J. K.; Fluitt, A. M.; Hoganson, A. J.; Moran, S. D.; de Pablo, J. J.; Skinner, J. L.; Zanni, M. T. Structural motif of polyglutamine amyloid fibrils discerned with mixed-isotope infrared spectroscopy. *Proc. Natl. Acad. Sci.* **2014**, *111*, 5796–5801.

(46) Strasfeld, D. B., Ling, Y. L.; Gupta, R.; Raleigh, D. P., Zanni, M. T. Strategies for Extracting Structural Information from 2D IR Spectroscopy of Amyloid: Application to Islet Amyloid Polypeptide. *J. Phys. Chem. B* **2009**, *113*, 15679–15691.

(47) Torii, H. Amide I Vibrational Properties Affected by Hydrogen Bonding Out-of-Plane of the Peptide Group. *J. Phys. Chem. Lett.* **2015**, *6*, 727–733.

(48) Walsh, S. T.; Cheng, R. P.; Wright, W. W.; Alonso, D. O.; Daggett, V.; Vanderkooi, J. M.; DeGardo, W. F. The hydration of amides in helices; a comprehensive picture from molecular dynamics, IR, and NMR. *Protein Sci.* **2003**, *12*, 520–531.

(49) Hundertmark, M.; Popova, A. V.; Rausch, S.; Seckler, R.; Hincha, D. K. Influence of drying on the secondary structure of intrinsically disordered and globular proteins. *Biochem. Biophys. Res. Commun.* **2012**, *417*, 122–128.

(50) Kwac, K.; Lee, H.; Cho, M. Non-Gaussian statistics of amide I mode frequency fluctuation of N-methylacetamide in methanol solution: Linear and nonlinear vibrational spectra *J. Chem. Phys*. **2004**, *120*, 1477-1490.

(51) Lomont, J. P.; Ostrander, J. S.; Ho, J. J.; Petti, M. K.; Zanni, M. T. Not All β-Sheets Are the Same: Amyloid Infrared Spectra, Transition Dipole Strengths, and Couplings Investigated by 2D IR Spectroscopy. J. Phys. Chem. B **2017**, *121*, 8935–8945.

(52) Kong, J.; YU, S. Fourier Transform Infrared Spectroscopic Analysis of Protein Secondary Structures. *Acta Biochimica et Biophysica Sinica* **2007**, *39*, 549–559.

(53) Sharma, C.; Srivastava, A. K.; Sharma, D.; Joshi, R. K. Iron- and copper-based bifunctional catalysts for the base- and solvent-free C–N coupling of amines and aryl/benzyl chlorides under aerobic conditions *New J. Chem.*, **2022**, ***46***, 8551-8556.

(54) Suh, M. J.; Kim, G.; Kang, J.; Lim, M. H. Strategies Employing Transition Metal Complexes To Modulate Amyloid-β Aggregation. *Inorg. Chem.* **2019**, *58*, 8–17.

(55) Faller, P.; Hureau, C .; Berthoumieu, Olivia, B. Role of Metal Ions in the Self-assembly of the Alzheimer's Amyloid-β Peptide. *Inorg. Chem.* **2013**, *52*, 12193–12206.

(56) Miura, T.; Suzuki, K.; Kohata, N.; Takeuchi, T. Metal Binding Modes of Alzheimer's Amyloid β-Peptide in Insoluble Aggregates and Soluble Complexes *Biochemistry* **2000**, *39*, 7024–7031.

TOC Entry